Superconformal film growth: Mechanism and quantification

T. P. Moffat
D. Wheeler
M. D. Edelstein
D. Josell

Superconformal electrodeposition of copper is explained by the recently developed curvature-enhanced-accelerator coverage (CEAC) model, which is based on the assumptions that 1) the local growth velocity is proportional to the surface coverage of the accelerator, or catalyst, and 2) the catalyst remains segregated at the metal/electrolyte interface during copper deposition. For growth on nonplanar geometries, this leads to enrichment of the catalyst on advancing concave surfaces and dilution on advancing convex sections, thereby giving rise to bottom-up superfilling of submicrometer trenches and vias. In this paper the robustness of the CEAC model is demonstrated by characterizing the kinetics of catalyst accumulation and consumption in a series of electroanalytical experiments on planar electrodes. The model is then used to successfully predict interface shape evolution during feature filling in a variety of experiments, without using adjustable parameters.

Introduction

State-of-the-art manufacturing of semiconductor logic and memory devices involves electrodeposition of copper for wiring. The process, pioneered by IBM, depends on the use of electrolyte additives that affect the local deposition rate, thereby resulting in superconformal, or bottom-up, "superfilling" of trenches and vias [1, 2]. In the early years, an understanding of superfilling technology lagged behind its implementation in manufacturing because of a combination of factors.

The first generation of electrolytes contained numerous components, and general knowledge of both the chemistry and processing conditions was significantly constrained by proprietary concerns. As a result, early modeling studies focused on traditional leveling theory, in which the location-dependent growth rate derived from diffusion-limited accumulation of an inhibiting species onto the metal surface [2–4]. In those studies it was necessary to empirically modify the area-blockage leveling theory in order to try to capture the experimentally observed shape-change behavior [2, 3]. Despite these modifications, studies of shape evolution of the growth front during feature filling and the observation of bump formation above the filled trenches made it clear that superfilling could not be rationalized by traditional transport-limited leveling models [5–7]. At the same time, simplification of electrolyte additive packages to two (accelerator, suppressor) and three (accelerator, suppressor, leveler) components opened the way for detailed studies of the filling process [8, 9]. Subsequently, a curvature-enhanced-accelerator coverage (CEAC) mechanism was shown to quantitatively describe the superconformal film growth that is responsible for bottom-up superfilling of submicrometer features in damascene processing [10–13]. The model also provides an explanation for the beneficial effects on roughness evolution induced by certain additives known as "brighteners" [14]. Moreover, the generality of the CEAC model has been demonstrated by successful application to silver electrodeposition [15] and copper chemical vapor deposition [16] for the filling of submicrometer features.

The main characteristic of two-component superfilling electrolytes is the competition between inhibitors and accelerators for electrode surface sites. A model "two-component" additive package for copper superfilling contains a mixture of a dilute (i.e., micromolar) accelerator such as SPS [$Na_2(S(CH_2)_3SO_3)_2$] in the presence of an inhibitor such as PEG (polyethylene

0018-8646/05/$5.00 © 2005 IBM

glycol, molecular weight = 3,400), which is typically an order of magnitude higher in concentration. Immersion of a copper electrode in the electrolyte results in the rapid formation of a thin passivating PEG-based film. The passivating layer is subsequently displaced or disrupted by the adsorption of the catalytic short-chain disulfide molecules. This results in an increase in the metal deposition rate that is a monotonic function of the catalyst coverage. Under certain conditions, activation of the metal deposition rate is sustained by the tendency of the catalyst to remain segregated on the growing interface. This combination of effects yields hysteretic voltammetric curves and rising chronoamperometric transients that enable quantification of the competitive adsorption process. Multicycle voltammetry reveals additional characteristics that reflect the significant potential dependence of catalyst adsorption as well as its subsequent deactivation.

This simple competitive adsorption model can give rise to a superconformal film growth mode via the CEAC mechanism. According to the CEAC formalism, deposition on a nonplanar surface, which is inherently accompanied by changes in the local surface area, affects the local adsorbate surface coverage in multicomponent systems. In the present case, the coverage of the more strongly bound catalytic species increases on advancing concave sections and decreases on advancing convex segments. Since the deposition rate is proportional to catalyst coverage, this naturally gives rise to bottom-up filling of features and, more generally, superconformal film growth. The CEAC model becomes increasingly applicable as the dimensions of the surface profile shrink into the submicrometer regime. To date, three different shape-change algorithms of varying complexity have been used to describe the filling of submicrometer features such as trenches and vias [10–l2]. The models successfully predict interface evolution from the initial incubation period of (near) conformal growth through superconforma1 "bottom-up" filling to "momentum plating," or bump formation over filled features.

In this paper, quantitative electroanalytical measurements on planar electrodes are used to parameterize the adsorbate kinetics for use in the CEAC model. The model is then applied, with no adjustable parameters, to three different feature-filling experiments. In the first example, the decisive role of a submonolayer catalyst coverage is demonstrated by superfilling trenches that were derivatized with catalyst prior to copper plating in a catalyst-free PEG–Cl electrolyte. Next, the filling of different-aspect-ratio trenches using a prototypical SPS–PEG–Cl electrolyte is examined. Finally, the filling of a cylindrical via geometry under the same deposition conditions is discussed.

Copper deposition mechanism and kinetics

Copper deposition in an acid sulfate and perchlorate medium has been widely studied using a variety of electroanalytical methods [17–24]. Two separate charge-transfer steps,

$$Cu^{++} + e \rightarrow Cu^{+} \quad (1)$$

and

$$Cu^{+} + e = Cu, \quad (2)$$

have been identified. The first reaction is rate-controlling, with the second step having a rate constant that may be up to three orders of magnitude greater [17, 20, 21]. The solvated Cu^{+} intermediate has been observed in a variety of rotating ring-disc measurements [17, 19, 20, 22], while an adsorbed Cu^{+} intermediate has been invoked to describe the impedance response during copper deposition [24, 25]. In fact, the equilibrium Cu^{+} concentration in the additive-free 0.24-mol/L $CuSO_4$/Cu system is of the order of about 400 μmol/L, significantly greater than the combined concentrations of all of the organic additives used in the superfilling electrolyte. The activity of the Cu^{+} intermediates can be significantly perturbed by complex formation with additive species; rotating ring-disc experiments reveal that the interfacial Cu^{+} concentration goes through a maximum at –0.02 V, with the magnitude being a strong function of electrolyte additives [22].

Additive effects

Inhibition by PEG–Cl

The addition of chloride to a cupric sulfate electrolyte is known to catalyze the rate-controlling Cu^{++}/Cu^{+} reaction, while PEG alone exerts a negligible influence on the deposition rate [25–30]. In contrast, the combination of PEG and Cl results in significant inhibition of the copper deposition reaction due to the formation of a PEG–Cl film that blocks the access of Cu^{++} to the surface [25–30]. The immersion of a freshly abraded copper surface into a copper-plating electrolyte containing concentrations of PEG and NaCl such as those given in **Table 1** results in the rapid formation of a PEG–Cl blocking layer. During steady-state metal deposition, mass conservation requires that the rate of adsorption and desorption or incorporation of PEG into the growing solid be balanced. Significantly, a recent SIMS study [31], combined with the absence of significant grain refinement in the copper deposits [8], indicates that negligible incorporation of the inhibiting PEG species into the metal deposit occurs during metal deposition in electrolytes containing only PEG–Cl.

Table 1 Composition of copper-plating electrolyte.

0.24 mol/L $CuSO_4$
1.8 mol/L H_2SO_4
1.0 mmol/L NaCl
88 μmol/L PEG (3,400 MW)
x μmol/L SPS (x = 0 to 500)

Voltammetric experiments in the presence of PEG–Cl yield a reduction of the deposition kinetics of nearly two orders of magnitude relative to that for an additive-free solution [25, 27, 30]. In previous work, the exponential increase of current on the inhibited surfaces with overpotential had been ascribed to an increase in charge-transfer rate occurring across a small fraction of mobile active surface sites. The extent of inhibition is quantified in terms of the effective activity or coverage, θ_{PEG}, of the blocking layer. For the purposes of this work, the voltammetric overpotential–current density (η–i) and chronoamperometric current density–time (i–t) behaviors observed with the PEG–Cl electrolyte are used to define the activity (i.e., $\theta_{PEG} = 1$) of the fully inhibited system that serves as the reference point for subsequent discussion of the effects of SPS adsorption.

Catalytic effect of SPS additions

SPS additions to the PEG–Cl electrolyte result in disruption of the PEG-based passivating layer and acceleration of the deposition reaction. This is evident from the hysteretic voltammetric curves shown in **Figure 1(a)**. The metal deposition rate at a given potential on the negative-going sweep increases with increasing SPS concentration. For the scan rate and switching potential employed here, the hysteresis is maximized for an SPS concentration near 2.59 μmol/L. Further additions of SPS result in progressively higher deposition rates on the negative-going potential sweep, while the response on the return scan is effectively saturated. The experiments, using freshly abraded copper electrodes (i.e., 400-grade SiC), are accompanied by significant brightening of the plated surface; the absence of roughening indicates that the hysteretic behavior must derive from a change in interfacial chemistry rather than surface area. **Table 2**, discussed in more detail later, shows the parameters and constants used to fit the simulated voltammetry curves shown in **Figure 1(b)**, which is also discussed later.

The response of the system to potentiostatic polarization was also investigated. In the absence of SPS, current transients such as that shown in **Figure 2(a)** are characterized by an approximately 30-s decay associated with establishing the hydrodynamic boundary layer that accompanies deposition proceeding under mixed control. For the catalyst-free PEG–Cl electrolyte, an additional

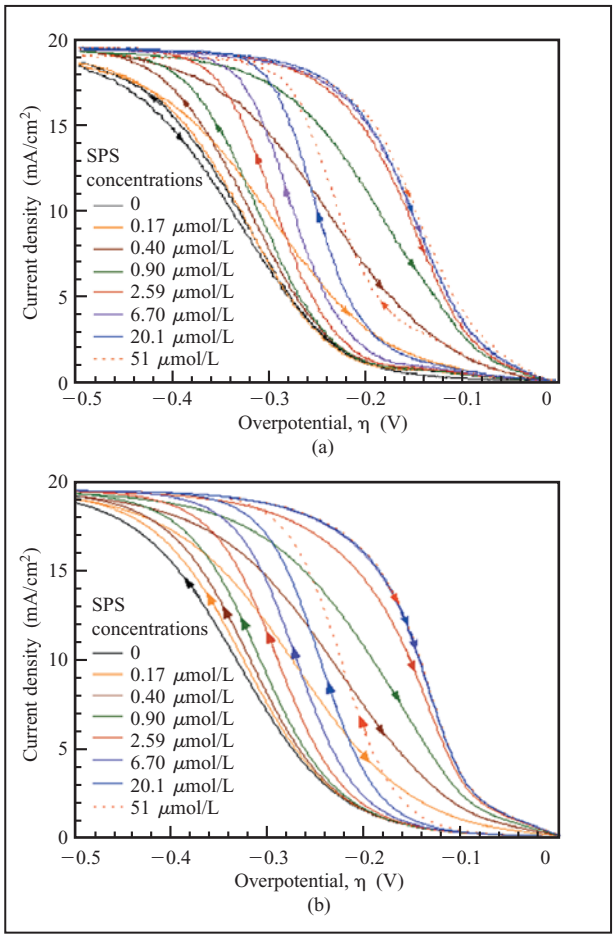

Figure 1

(a) Hysteretic voltammetry curves, reflecting the displacement of inhibiting PEG–Cl species by adsorption of SPS at different concentrations. The bath components are as given in Table 1; the scan rate was 1 mV/s for the stationary copper electrode. (b) Results of simulations based on the competitive adsorption model using the parameters and constants listed in Table 2.

relaxation occurs that is not complete until about 400 s. This is associated with a slight increase in the blocking character of the PEG–Cl film. This effect is manifested in the voltammetric experiment as the attenuation of the small wave centered at –0.14 V upon cycling the potential. Part (b) of Figure 2 is discussed later.

In contrast, addition of SPS to the fully inhibited PEG–Cl system results in rising current transients. After an initial decay of approximately 30 s, the current increases in a manner that corresponds qualitatively to following a vertical trajectory across the hysteretic η–i curves shown in Figure 1(a). For the given overpotential, the rise time decreases monotonically with SPS concentration, as seen in Figure 2(a).

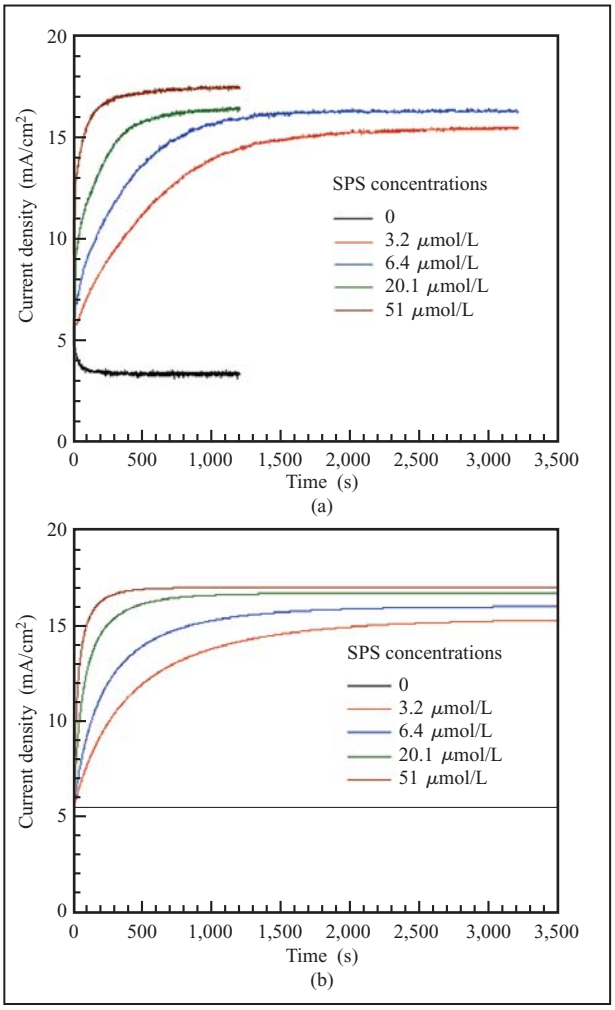

Figure 2

(a) Rising chronoamperometry transients characterizing the activation of PEG–Cl-inhibited electrodes induced by SPS adsorption on stationary copper electrodes at −0.25 V. (b) Results of simulations based on the competitive adsorption model using the parameters and constants listed in Table 2.

Table 2 Parameters and constants used to obtain the simulation results shown in Figures 1(b) and 2(b).

Metal deposition parameters obtained from experiments on planar electrodes.			
i^0_{PEG}	(mA/cm^2)	0.03 (i–t)	0.015 (i–η) (see text)
i^0_{SPS}	(mA/cm^2)	2.25	
α_{PEG}		0.5	
α_{SPS}		0.4	
$D_{Cu^{++}}$	(cm^2/s)	4×10^{-6}	(from [22])
δ	(cm)	0.00987	
Ω	(cm^3/mol)	7.1	
Catalyst adsorption and consumption parameters obtained from experiments on planar electrodes.			
k_0	(cm^{3}s/mol)	260	
α_{ads}		0.6	
D_{SPS}	(cm^2/s)	4×10^{-6}	
Γ^0	(mol/cm^2)	6.35×10^{-10}	
m	(V^{-1})	4	
b		2.65	
A	(s^{-1})	0.3	
B_a	(V^{-1})	−35	
B_b	(V^{-1})	60	
B_d	(s^{-1})	0.0008	
V_d	(V)	0.095	
Constants			
R	(J/Kmol)	8.314	
T	(K)	298	
F	(C/mol)	96,485	

For both η–i and i–t experiments, the electrochemical response may be simply modeled in terms of disruption of the rapidly formed PEG–Cl blocking layer by more gradual SPS adsorption. Activation by SPS may manifest itself in at least two ways; disulfide or thiolate adsorption can displace some of the "co-inhibitor" chloride from the copper surface, and the charged sulfonate terminal group disrupts and prevents reformation of the passivating PEG-based layer. The extent of disruption is a monotonic function of the catalyst coverage, θ_{SPS}.

The important role of the sulfonate end group is demonstrated by examining the rate of copper deposition on various catalyst-derivatized electrodes in a catalyst-free PEG–Cl electrolyte [30]. On the basis of solubility concerns, the electrodes were derivatized for 60 s in either an ethanolic or 1.8-mol/L H_2SO_4 aqueous solution containing a 1-mmol/L concentration of the molecule of interest. As shown in **Figure 3**, thiols or disulfides with a charged sulfonate terminal group yield significant and sustained catalysis of the metal deposition rate, indicating that they remain on the surface of the deposit and prevent formation of the passivating PEG–Cl film. In contrast, electrodes derivatized with molecules containing alternative end groups result in increased inhibition. In the case of CH_3-terminated molecules, the increased inhibition is sustained for hundreds of seconds,

while electrodes modified with –OH or –COOH terminal groups are quickly deactivated, presumably by incorporation of the molecules into the growing solid.

Experiments were performed to characterize the catalyst consumption kinetics independently of the ambiguities associated with the adsorption process [30]. Chronoamperometric experiments revealed that electrodes derivatized for 60 s in 0.5 mmol/L SPS exhibit notable resilience against passivation by PEG–Cl, particularly at higher overpotentials (**Figure 4**). For comparison, transients for freshly abraded electrodes show the baseline toward which the behavior of the modified electrodes evolves as the catalyst is consumed. Deactivation at –0.05 V occurs with a time constant of about 200 s, while at –0.25 V significant catalysis is sustained for a period that is at least an order of magnitude longer. The ability of the catalyst to remain on the surface during rapid metal deposition indicates that it is able to rapidly segregate, or "float," on the growing metal surface. In contrast, the more rapid consumption at slower growth rates suggests a competing chemical reaction as the origin for the deactivation process. The –0.25-V case corresponds to the potential used in most feature-filling experiments; the data indicates that only minor deactivation, or consumption, occurs on the <100-s time scale of feature filling. This is congruent with the second tenet of the CEAC model, namely that the catalyst remains segregated on the growth surface.

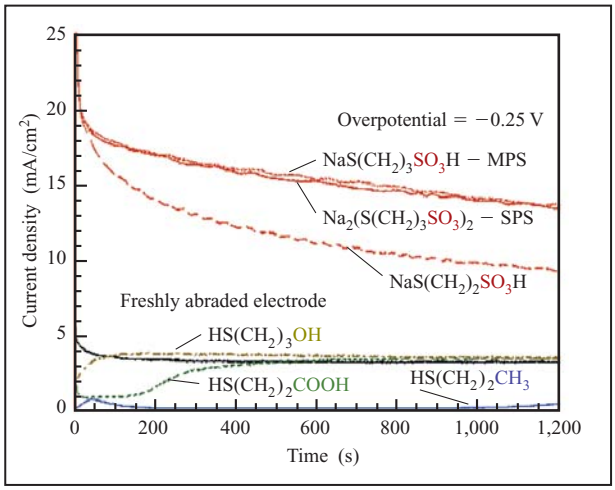

Figure 3

Chronoamperometry transients establishing the catalytic behavior of sulfonate terminal groups (red) in contrast to the inhibition provided by the (OH, COOH, CH_3) terminal groups.

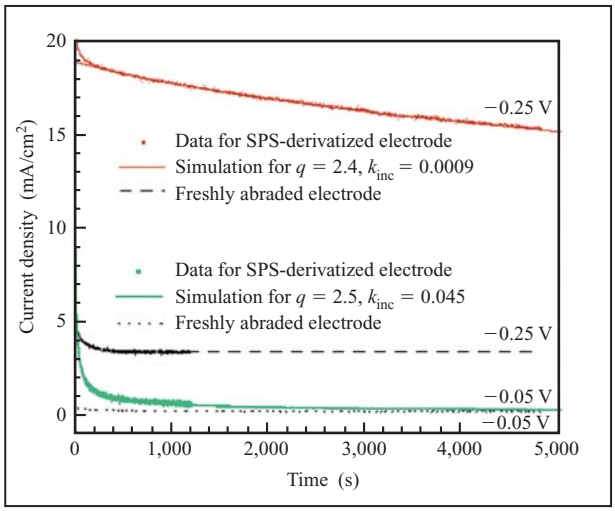

Figure 4

Chronoamperometry behavior for stationary copper electrodes, showing the catalytic effect of SPS derivatization and its persistence. At large overpotential (−0.25 V), corresponding to practical plating conditions, the catalytic effect is sustained for thousands of seconds. In contrast, at smaller overpotential (−0.05 V) the derivatized electrode is subject to more rapid deactivation. The solid curves correspond to model fits yielding the q (power-law consumption) and k_{inc} (SPS incorporation rate constant) parameters shown in Figure 5.

Microstructural effects

Additive incorporation exerts a strong influence on microstructural evolution, e.g., grain refinement, and the resulting physical properties of the deposit. Integration of the chronoamperometric transients for SPS-derivatized electrodes allows the level of SPS incorporation to be estimated. Assuming that the full monolayer of catalyst is incorporated (i.e., no desorption) and using the still incomplete deactivation transients shown in Figure 4 to obtain the deposit thickness yields a conservative (upper-bound) estimate of the impurity levels. The sulfur content in the deposit is estimated to be 4 ppm S and 200 ppm S for growth at –0.25 V and –0.05 V, respectively. The potential dependence and magnitude are in good agreement with published secondary ion mass spectroscopy (SIMS) data on impurity content [32–34]. However, unlike the derivatization experiments shown here, interpretation of previous SIMS experiments is limited by the need to deconvolute the catalyst adsorption and deactivation processes.

Modeling competitive adsorption and its effect on copper deposition

The central role of the SPS-based catalyst is to open channels in the PEG–Cl blocking layer, thereby allowing the Cu^{++}/Cu^{+} reaction to proceed unhindered. This effectively accelerates the metal deposition reaction without requiring any change in the Cu^{++}/Cu^{+} reduction mechanism, i.e., activation of a blocked electrode.

Accelerated copper deposition occurs in the proximity of SPS adsorption sites. Chloride adsorbed in neighboring sites may also exert its well-known catalytic properties for copper deposition, thereby expanding the effective area catalyzed. Nonetheless, for simplicity, the total number of available surface sites is taken here as the sum of the coverage of the inhibiting PEG–Cl species, θ_{PEG}, and the catalytic SPS–Cl species, θ_{SPS},

$$\theta_{SPS} + \theta_{PEG} = 1. \quad (3)$$

Saturation surface site density

Chloride is known to form compact ordered monolayers on copper surfaces under open circuit conditions in simple halide solutions, e.g., c(2×2) Cl on Cu(100) [35]. However, little is known concerning the adsorption geometry of the inhibiting PEG–Cl complex. In contrast, SPS adsorbs on copper surfaces either directly as disulfide or dissociatively as two thiolate molecules. In either case, one SPS molecule ends up occupying two sites on the metal surface (see for example [36, 37]). A mechanically polished, annealed copper-plate electrode was used for the electroanalytical kinetic studies. The rolling and annealing process produces a (200) texture; thus, the surface coverage used for simulations was indexed to Cu(100)—namely, 2.55×10^{-9} mol/cm^2. Studies of methanethiolate, dimethyl disulfide, ethanethiolate, heptanethiolate, and hexanethiolate adsorption on Cu(100) indicate that defected c(2×2) and c(2×6) thiolate adlayers are formed corresponding to a proportional surface coverage between 0.5 and 0.3 of a monolayer with respect to the underlying copper atoms [38–40]. In other studies of functionalized alkanethiol monolayers on Au(111) electrodes, the size of the terminal group, together with the chemical interaction between neighboring thiol molecules, was found to play an important role in the resulting structure; short-chain thiols with bulky end groups often yield lower-density coverages and distorted packing arrangements [41]. Pending further study of the structure of saturated monolayers of SPS or MPS [$NaS(CH_2)_3SO_3H$], as well as mixed monolayers of SPS–Cl and MPS–Cl on various copper surfaces, the c(2×2) structure will be taken as an upper-bound estimate for the saturated surface coverage, Γ^0, corresponding to a value of 6.35×10^{-10} mol/cm^2, since one SPS molecule occupies two sites.

Site dependence of charge-transfer kinetics

The effect of the adsorbates on the kinetics of the copper deposition reaction is described as the product of the fractional interface cupric ion concentration $C_{Cu^{++}}/C^{\infty}_{Cu^{++}}$ (where $C^{\infty}_{Cu^{++}}$ denotes the bulk concentration) and the coverage-dependent charge-transfer-rate constants k_j using

$$i(\theta_{SPS}, \eta) = \frac{C_{Cu^{++}}}{C^{\infty}_{Cu^{++}}}[k_{PEG}(1 - \theta_{SPS}) + k_{SPS}\theta_{SPS}], \quad (4)$$

where

$$k_j = 2i^0_j\left[\exp\left(\frac{-\alpha_j F\eta}{RT}\right) - \exp\left(\frac{(1-\alpha_j)F\eta}{RT}\right)\right], \quad (5)$$

and the subscript j pertains to the PEG–Cl or SPS–Cl saturated surface. The exchange i^0_j corresponds to the rate-determining step for copper deposition on PEG or SPS surface sites, and a factor of 2 is used to account for the overall two-electron Cu^{++}/Cu process. The values of i^0_{PEG} and the transfer coefficient α_{PEG} were readily determined from η–i and i–t experiments performed in the catalyst-free PEG–Cl electrolyte. Evaluation of i^0_{SPS} and α_{SPS} was more difficult; it involved examining the response of an SPS-derivatized electrode in the same PEG–Cl catalyst-free electrolye, with appropriate consideration given to catalyst consumption as described later.

Under steady-state hydrodynamic conditions, the interface concentration of Cu^{++} can be related to the diffusion-limited current density i_L. This, in turn, is related to the boundary layer thickness δ, which, in our experiments, was established by natural convection associated with the Cu^{++} depletion gradient. Taken together,

$$\frac{C_{Cu^{++}}}{C^{\infty}_{Cu^{++}}} = 1 - \frac{i}{i_L} \quad \text{and} \quad i_L = \frac{2FD_{Cu^{++}}C^{\infty}_{Cu^{++}}}{\delta}, \quad (6)$$

where F is Faraday's constant and $D_{Cu^{++}}$ is the cupric ion diffusion coefficient.

Catalyst evolution

Evolution of the catalyst on a planar surface entails a balance between SPS adsorption and consumption. This is quantified by using the effective rate constants for SPS adsorption, k_{ads}, and incorporation, k_{inc}, with a power-law consumption exponent q. For catalyst precursor concentration, C_{SPS}, one obtains

$$\frac{d\theta_{SPS}}{dt} = k_{ads}(1 - \theta_{SPS})C_{SPS} - k_{inc}\theta^q_{SPS} \quad (7)$$

at the planar metal/electrolyte interface.

SPS adsorption from the electrolyte

In an electrolyte containing a dilute SPS concentration, the occurrence of disulfide adsorption is coincident with displacement of the less strongly bound PEG-based inhibitor. The adsorption or exchange process is assumed to be described by irreversible Langmuir kinetics [42–44].

The effective rate constant, k_{ads}, is potential-dependent, the rate increasing exponentially with overpotential η according to

$$k_{ads} = k_0 \exp\left(-\frac{\alpha_{ads} F\eta}{RT}\right). \quad (8)$$

The symmetry of the activation barrier, α_{ads}, and the pre-exponential term, k_0, are determined by fitting the experimental η–i curves on the planar substrates over the range of SPS concentration [see for example Figure 1(b)]. The potential dependence requires further comment.

Potential-dependent halide adsorption, including order–disorder phenomena, is well known [35], and it is reasonable to surmise that the breakdown of the PEG–Cl blocking layer might also be potential-dependent. In a similar fashion, the composition and structure of thiols and disulfides adsorbed on gold from simple electrolytes have been shown to be potential-dependent [45]. In the present case, it is also possible that the approach of SPS to the electrode surfaces is screened by complexation with Cu^+ that is generated at the electrode. As noted earlier, the equilibrium Cu^+ concentration in the additive-free system [i.e., Equations (1) and (2)] is of the order of about 400 μmol/L, and Cu^+ is thought to form complexes with all of the additives under consideration [19, 22, 27, 28]. According to Equation (2), the equilibrium Cu^+ concentration decreases exponentially with potential, i.e., 60 mV per decade of concentration. Thus, the increasing rate of SPS adsorption with overpotential may partly reflect the strong decrease in the interfacial Cu^+ concentration that otherwise scavenges SPS (as well as chloride, oxygen, etc.) as it approaches the interface. Further work will be required to elucidate the relative contributions of these processes to the potential dependence of k_{ads}.

Since the rate constant k_{ads} increases rapidly with overpotential, the adsorption process must eventually become constrained at higher overpotentials by the diffusion of SPS in the electrolyte, characterized by its diffusion coefficient D_{SPS}. The mass balance for catalyst accumulation on the interface from the electrolyte is given by

$$k_{ads}(1-\theta_{SPS})C_{SPS} = \frac{D_{SPS}}{\Gamma_0}\frac{(C^{\infty}_{SPS} - C_{SPS})}{\delta}. \quad (9)$$

Rearranging the equation, one obtains the interface SPS concentration,

$$C_{SPS} = \frac{C^{\infty}_{SPS}}{1 + \dfrac{k_{ads}\Gamma_0\delta(1-\theta_{SPS})}{D_{SPS}}}, \quad (10)$$

which is to be used in Equation (7).

SPS consumption

The stability of the catalyst is determined by its propensity to remain segregated on the moving interface rather than being incorporated into the growing deposit. The partitioning of the adsorbate is determined from the kinetics of copper deposition on SPS-derivatized electrodes in an SPS-free PEG–Cl electrolyte. As shown by the solid lines in Figure 4, the decaying current transients associated with catalyst consumption can be modeled as a higher-order reaction, i.e., with exponent $q > 1$, in catalyst coverage [see Equation (7)]. This implies significant lateral interactions between catalyst molecules that might represent the first stage of copper sulfide formation. The values of the reaction order q and the rate constant k_{inc} obtained from fitting the data are dependent on the values of α_{SPS} and i^0_{SPS}; these are discussed later. Transients from four different series of experiments were fit to determine q and k_{inc}. The former decreases with potential and is modeled in **Figure 5(a)** as a linear function,

$$q = m\eta + b. \quad (11)$$

The latter exhibits a more complicated potential dependence, passing through a maximum near –0.1 V [**Figure 5(b)**]. The potential dependence of the rate constant is described by the generalized asymmetric peak function,

$$k_{inc} = B_d + \frac{A}{\exp(-B_a[\eta + V_d]) + \exp(B_b[\eta + V_d])}, \quad (12)$$

with the coefficients A, B_a, B_b, B_d, and V_d being determined by fitting the data in Figure 5(b). As is evident in Figure 5, significant dispersion exists between the different series of experiments; at certain potentials, values of k_{inc} span an order of magnitude. Since reproducibility within each series of experiments was quite favorable, the source of dispersion is most likely related to uncontrolled details of the derivatization experiments, possibly including the effects of unintended chloride co-adsorption in the different experiments. The need for more refined data is evident, as the scatter in q and k_{inc} remains the chief impediment to a more precise description of the deposition kinetics. Nevertheless, the experiments provide an order of magnitude estimate of the consumption parameters and, equally important, reveal the potential dependence of the catalyst deactivation process. The potential dependence is arguably counterintuitive, since the maximum deactivation rate occurs when the growth rate is low. Interestingly, rotating ring-disc studies of copper deposition reveal that the interfacial concentration of solvated Cu^+ intermediate goes through a maximum at a small overpotential of about –0.02 V and falls below the experimental background by about –0.15 V [22]. The

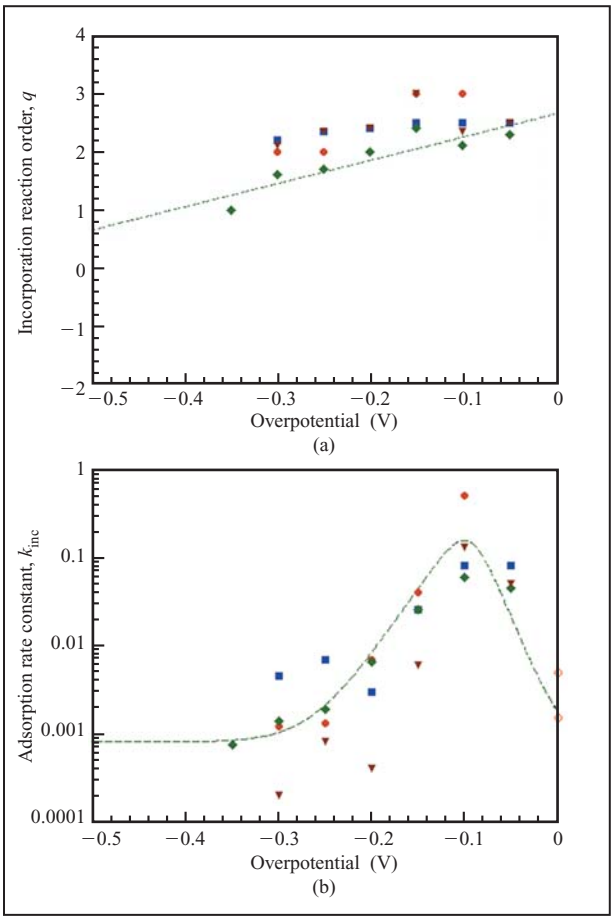

Figure 5

(a) Incorporation reaction order and (b) adsorption rate constant vs. overpotential, as determined from fits to chronoamperometric transients (e.g., the solid curves shown in Figure 4). Four different data sets are denoted by color. The dashed green curves indicate the functional forms of the parameters used in the simulations of Figures 1(b) and 2(b).

similarities of the potential dependencies suggest that the enhanced consumption process at small overpotentials might be coupled with Cu^{+} activity at the interface.

Parameter selection and evaluation

The values for i^0_{PEG} and α_{PEG} are determined by fitting the η–i and i–t data for deposition in catalyst-free electrolyte containing PEG–Cl. As shown in **Figure 6**, the shape of the voltammetric curve is reasonably well described by $i^0_{PEG} = 0.016$ mA/cm^2 and $\alpha_{PEG} = 0.5$. The value of α_{PEG} is consistent with Cu^{++}/Cu^{+} reduction being the rate-determining step. No attempt was made to describe the small peak evident at low overpotentials, nor the slightly diminished current on the return sweep that is associated with some relaxation of the PEG–Cl blocking layer.

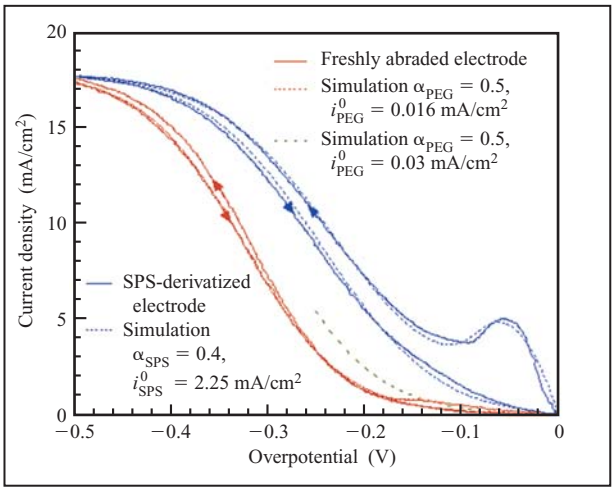

Figure 6

Voltammetry (1 mV/s) of copper deposition from the PEG–Cl electrolyte using a freshly abraded stationary copper electrode and an SPS-derivatized electrode (solid curves). The dashed curves correspond to the fits used to obtain the four parameters, i^0_{PEG}, α_{PEG}, i^0_{SPS}, and α_{SPS}.

Examination of the PEG–Cl i–t transient [Figure 2(a)] revealed that the relaxation process is not complete until about 400 s. This time-dependent increase of the inhibition is all but lost in the 1200-s-long voltammetric study, in which significant current is evident only after 100 s or more. However, the relaxation was clearly relevant during the time frame of feature-filling experiments. Correct analysis will require a robust description of this relaxation process. For the purposes of this paper, $i^0_{PEG} \approx 0.03$ mA/cm^2, estimated from the transient current values observed at 30 s [Figure 2(a)], was used rather than the value, 0.016 mA/cm^2, determined from the η–i results. This is long enough for the hydrodynamic boundary layer to be established, but still short compared to the full relaxation time. This choice has a negligible effect on the predicted long-time behavior of the full SPS–Cl–PEG system while greatly improving the simulation of the early-time i–t response. Consistently, the dashed green curve in Figure 6 reveals that the use of i^0_{PEG} thus determined yields a reasonable prediction of the peak current associated with the relaxation observed at –0.14 V.

The value for i^0_{SPS} was estimated by fitting the η–i curve for copper deposition on an SPS-derivatized electrode in the same PEG–Cl electrolyte. As seen in Figure 6, the η–i curve exhibits a distinct peak at 0.05 V that reflects the onset of significant consumption of the catalyst as described above (see Figures 4 and 5). The magnitude of the peak was found to effectively saturate for

derivatization treatments of 60 s or longer in either 0.5-mmol/L SPS or 1-mmol/L MPS. Thus, the initial derivatized catalyst coverage, θ_{SPS}, is taken to be unity in those cases. The limited potential range prior to the onset of significant consumption prevents an unambiguous determination of the transfer coefficient α_{SPS} and, thus, i^0_{SPS}. Nevertheless, working from the premise that the copper deposition mechanism is largely unaltered by adsorbed thiol, α_{SPS} was initially constrained to be between 0.4 and 0.6, which yields an estimate of 5.0 to 4.0 mA/cm^2 for i^0_{SPS}. A more robust description was obtained by noting that i^0_{SPS} and α_{SPS} exert a strong influence on the magnitude of the consumption parameters, k_{inc} and q (Figure 5), which are derived from fitting the current transients shown in Figure 4. Iteratively fitting all of the voltammetry and chronoamperometry data for SPS-derivatized electrodes yields a set of values for i^0_{SPS}, α_{SPS}, k_{inc}, and q that simultaneously provide a good description of all of the experimental results (see for example Figures 4 and 6).

With the parameters i^0_{PEG}, α_{PEG}, i^0_{SPS}, α_{SPS}, $k_{inc}(\eta)$, and $q(\eta)$ derived from experiments using either freshly abraded or SPS-derivatized electrodes in catalyst-free PEG–Cl, the hysteretic η–i data for the full SPS–PEG–Cl electrolyte were used to fit the catalyst adsorption parameters k_0 and α_{ads}. The negative-trending voltammetric sweep is particularly sensitive to the adsorption parameters, while the saturated return scan is dominated by the potential dependence of catalyst consumption, k_{inc}. The parameters and constants in Table 2 (with the exception of the i^0_{PEG} value discussed earlier) were used to fit the chronoamperometry results shown in Figure 2.

It should be noted that the parameters in Table 2 are not unique. The scatter in experimental consumption transients allows an equally good fit to the η–i and i–t SPS–PEG–Cl data to be obtained using a range of k_{inc} and q parameters, including even a fit of all of the consumption transient using a potential independent q value, e.g., $q = 2.5$. Further study and refinement of the derivatization procedure should help clarify the source of the experimental dispersion. It is also noteworthy that certain combinations of parameters yield distinct predictions for the catalyst evolution, and a variety of surface-analytical experiments are underway to help narrow the selection. Despite these uncertainties, a correct description of the SPS–PEG–Cl system clearly includes a deactivation process. This conclusion is reinforced by multicycle voltammetry, in which the potential dependence of adsorption, which is most significant at large overpotentials, is convolved with consumption that dominates catalyst evolution at low overpotentials.

Multicycle voltammetry

As shown in **Figure 7**, repetitive potential cycling reveals that the second and subsequent negative-trending sweeps do not follow the path of the preceding return sweep beyond –0.05 V. This is necessarily due to significant deactivation starting by this overpotential. A steady-state η–i response is generally attained by completion of the second cycle, although the precise number of cycles depends on the SPS concentration as well as other parameters—switching potential, scan rate (not shown), etc. The impact of the potential dependence of the adsorption rate constant is most clearly revealed by changes in the switching overpotential; the sweep rate (1 mV/s) and total scan time (2,400 s) were held constant. The high metal deposition rate that characterizes the return sweep for a switching overpotential of –0.45 V is not accessible if the sweep is reversed at less than –0.25 V. Voltammograms at intermediate values are consistent with this trend. These results demonstrate that the rate of displacement of the inhibiting PEG–Cl layer by SPS adsorption is an increasing function of overpotential; voltammetric cycling to larger overpotentials permits a larger increase in the catalyst surface coverage that manifests as higher currents on the return sweep.

CEAC mechanism and feature filling

Movement of a nonplanar interface necessarily causes changes in the local area that can affect its surface chemistry. For example, on concave portions of an advancing surface, the local area decreases during growth. In a system saturated with two or more adsorbates, this results in expulsion of the less strongly bound surface species, either by desorption into the electrolyte or by incorporation into the growing solid. In a related way, expansion of the surface at convex portions results in dilution of the existing adsorbates and opens up new surface sites to competitive adsorption of electrolyte species. Changes in the local coverage of the more strongly bound adsorbate may be described as the product of its local coverage, θ_{SPS}, curvature, κ, and interface velocity, v. A general statement of catalyst evolution on the moving interface includes SPS adsorption, consumption, and the area change effects associated with the interface motion. These are denoted, in order, by the terms on the right-hand side of the equation,

$$\frac{d\theta}{dt} = k_{ads}(1-\theta_{SPS})C_{SPS} - k_{inc}\theta^q + v\kappa\theta_{SPS}. \quad (13)$$

For superfilling applications, the last term should dominate system behavior. As outlined above, electroanalytical and surface-analytical measurements on planar electrodes, for which $\kappa \approx 0$, allow the adsorption and consumption parameters to be determined. Shape-

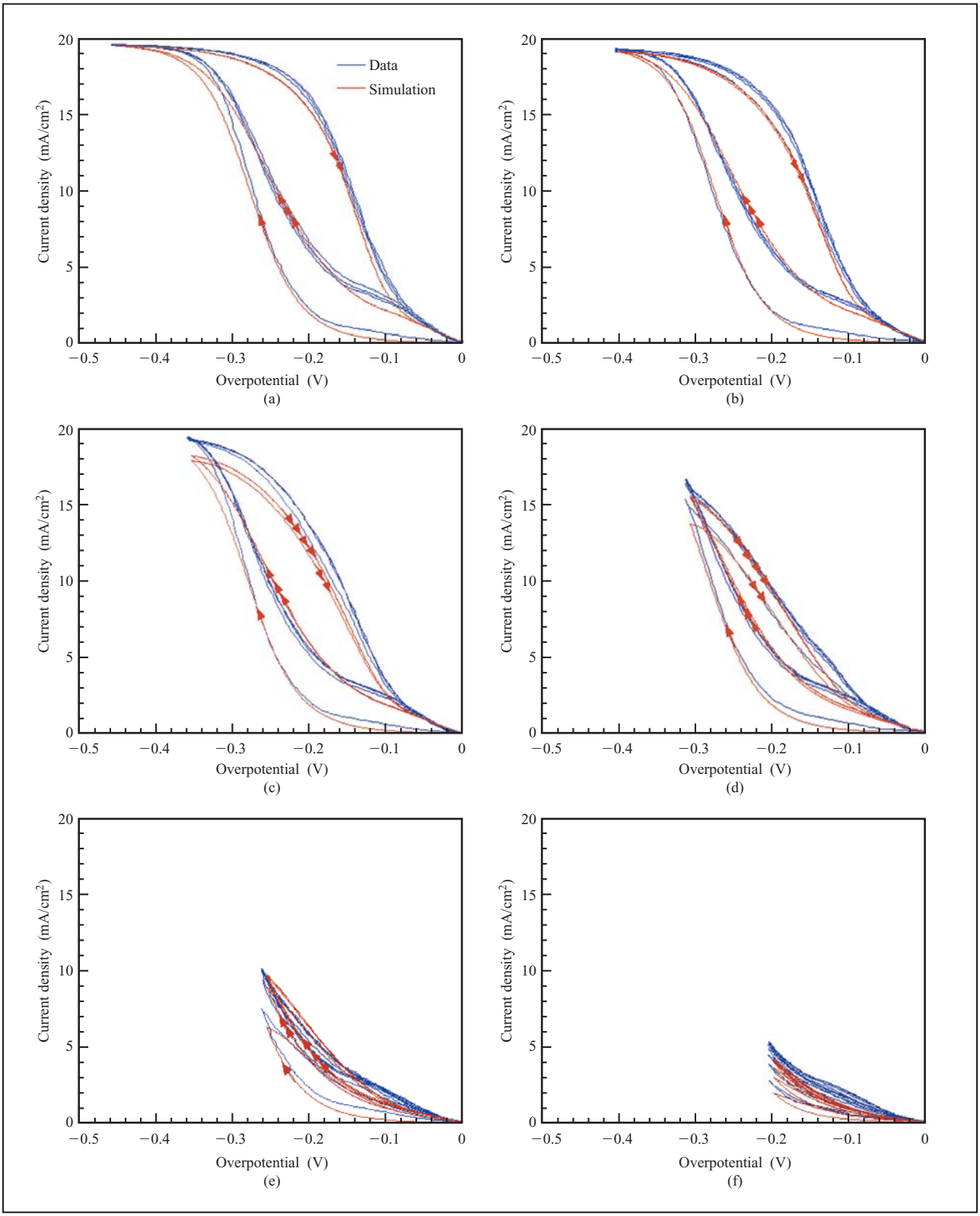

Figure 7

Variation of the voltammetric switching potential, revealing the strong effect of potential-dependent adsorption and consumption of the catalyst.

change simulations involve simply using the same equation, with κ being specified by the surface profile.

Superconformal deposition in trenches using catalyst-derivatized electrodes

The most dramatic and unambiguous demonstration of the CEAC mechanism is provided by superfilling of submicrometer features in a two-step process that involves derivatization of a patterned copper seed layer with a submonolayer quantity of catalyst, followed by copper plating in a catalyst-free electrolyte that contains PEG–Cl [46].

Experiment

The interface evolution during feature filling was examined for five different catalyst pretreatments. Derivatization involved 30-s immersion of the patterned electrode in a stagnant 1.8-mol/L H_2SO_4 solution containing 0.5, 5, 50, 500, or 1,000 μmol/L of the catalyst precursor, either SPS or MPS, followed by rinsing with water and drying with a tetrafluoroethane duster. Copper deposition was performed at an overpotential of −0.25 V in the SPS-free electrolyte. The specimens were plunged into the electrolyte with the potential applied, and the working electrode lead was immediately stabilized by clipping to the side of the vessel, thereby allowing a steady-state hydrodynamic boundary layer to develop with deposition time. After plating for the indicated time, the samples were cross-sectioned and ion-polished for imaging in a field-emission scanning electron microscope (FE–SEM). In the following discussion, specimens are identified by the catalyst precursor concentration used in the derivatization step.

Analysis of the filling images shown in **Figure 8** reveals several distinct and important phenomena. The acceleration of the deposition rate provided by the disulfide (or thiolate) catalysts is evident from the decrease in the feature filling time from approximately 200 s for specimens derivatized in 0.5-μmol/L SPS to approximately 40 s for derivatization in 500-μmol/L SPS. For the specimens derivatized in 0.5-μmol/L SPS, deposition proceeds conformally and the surface roughens with increasing film thickness. Eventually, this results in void formation, when the sidewalls impinge and a deep cusp forms above the trench. Identical behavior was observed for substrates which had not been derivatized, i.e., $\theta_{SPS} = 0$ (not shown). For the 5-, 50-, and 500-μmol/L SPS derivatizations, the initial increment of growth is still effectively conformal. However, it is followed by accelerated growth at the bottom concave corners that is characteristic of the inception of superconformal deposition. This yields the V-shaped bottom profile visible in the specimens plated for 70 s, 40 s, and 20 s, following derivatizations in 5-, 50-, and

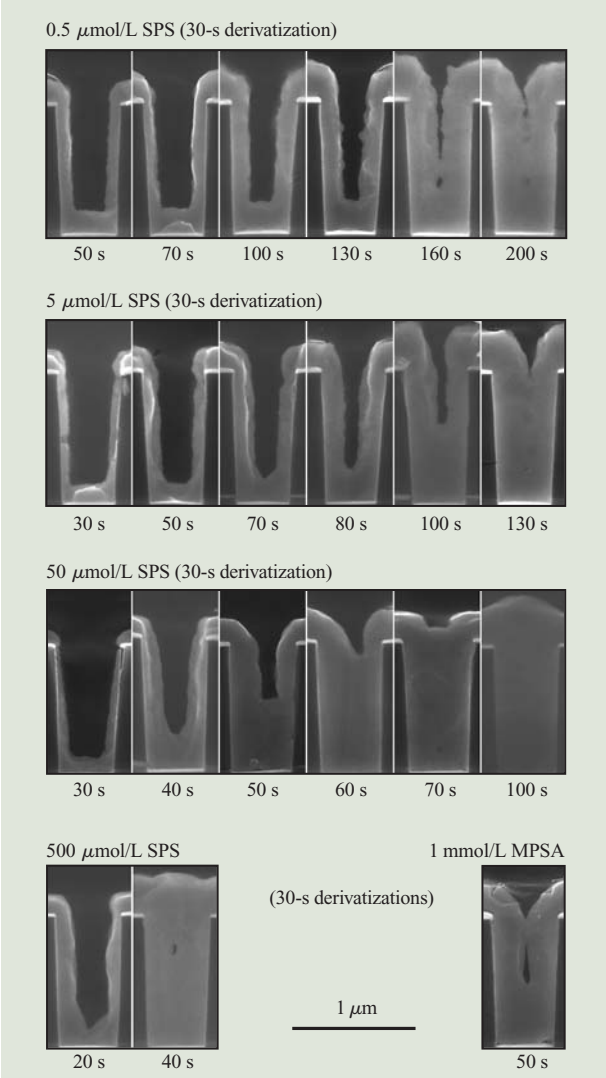

Figure 8

Superfilling of trenches pretreated with catalyst prior to copper plating in a PEG–Cl electrolyte at −0.25 V. The conditions used for electrode derivatization are indicated.

500-μmol/L SPS, respectively. Subsequently, catalyst enrichment at the apex of the V-shaped bottom leads to further acceleration and conversion to a flat-bottom profile. Between 80 s and 100 s, the specimens derivatized in 5 μmol/L exhibit rapid bottom-up filling, the hallmark of the "superfilling process." However, at about 130 s, the sidewalls impinge just before the rapidly advancing trench bottom reaches the top of the feature. In contrast, the 50-μmol/L specimens exhibit near-optimum superfilling behavior, with rapid bottom-up filling occurring between 50 and 70 s with negligible sidewall motion. An inversion of the growth front curvature is evident at 70 s, and by

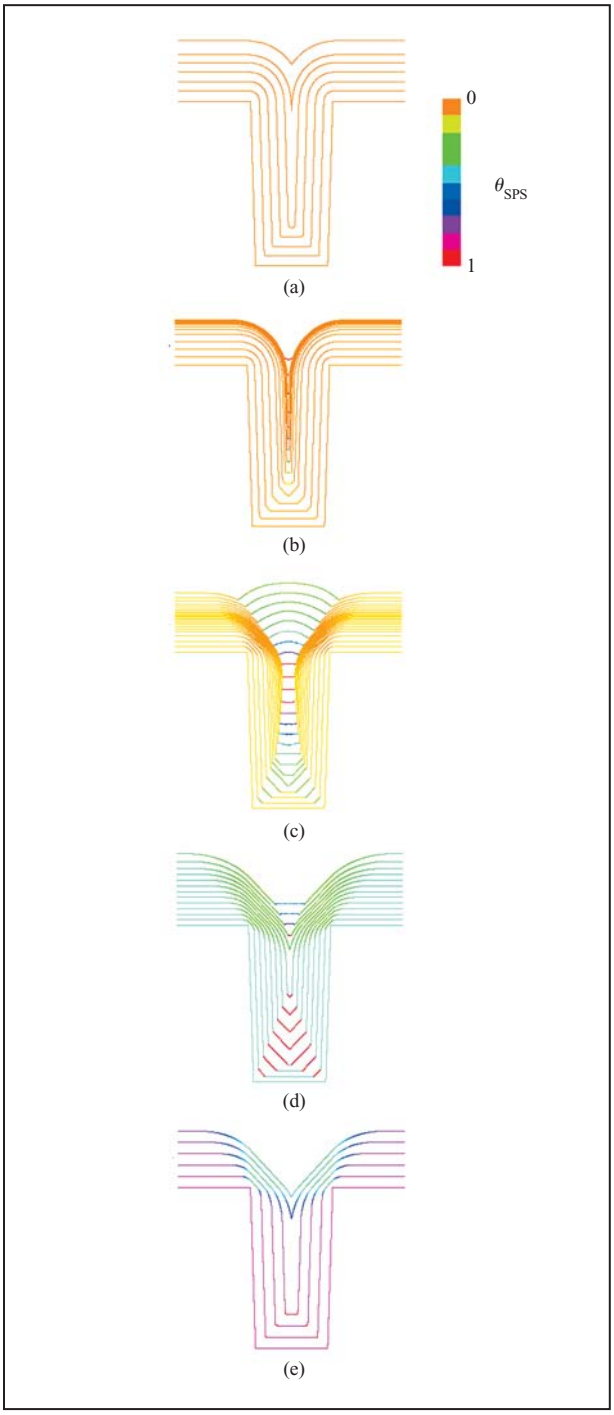

Figure 9

Simulations of feature filling using catalyst-pretreated electrodes. Interface motion is displayed using colorized contour lines to reflect the local catalyst coverage. Each simulation corresponds to a different initial catalyst coverage, $\theta_{SPS}^{t=0}$: (a) 0.00054; (b) 0.0054; (c) 0.054; (d) 0.44; and (e) 0.88 (comparable to the derivatization treatments specified in Figure 8). The feature-filling times corresponding to the last growth contour shown are (a) 177 s; (b) 113 s; (c) 85 s; (d) 39 s; and (e) 24 s.

100 s a large bump is seen above the trench. For the 500-μmol/L SPS and 1-mmol/L MPS specimens, void formation is clearly evident, this being more severe in the latter case. These experiments provide the strongest evidence that, in accordance with the CEAC mechanism, superconformal filling of submicrometer features derives chiefly from the evolution of a submonolayer quantity of a surface-confined catalyst, rather than through transport or chemistry within the electrolyte.

Simulation

Shape-change simulations based on the CEAC model are shown in **Figure 9**. They were implemented using an interface tracking code [10]. The electrolyte/metal interface at different stages of filling is delineated using contour lines that are colorized to reflect the local catalyst coverage. With increasing coverage, the colors range from orange ($\theta_{SPS} = 0$) through yellow, green, blue, and red ($\theta_{SPS} = 1$). The simulations use the cupric ion concentration at the surface that is reduced from the bulk concentration consistent with mass balance between the growing free surface and the cupric ion flux diffusing across a fixed hydrodynamic boundary layer. The cupric ion concentration is expressed as

$$C_{Cu^{++}} = C^{\infty}_{Cu^{++}} - \frac{\delta v}{\Omega D_{Cu^{++}}}, \tag{14}$$

where v is the surface growth velocity and Ω is the specific volume of copper. Depletion within the trench is ignored; the consequences of this are discussed below. The kinetic parameters, given in Table 2, are identical to those used to simulate the chronoamperometric results shown in Figure 2. The initial thiolate coverages of the SPS-derivatized electrodes, also required for the simulations, can be estimated from surface-analytical measurements.[1] Derivatization for 30 s in 0.5-, 5-, 50-, or 500-μmol/L SPS or 1,000-μmol/L MPS yields initial fractional catalyst coverages of approximately 0.00054, 0.0054, 0.054, 0.44, and 0.88, respectively, as shown in the corresponding simulations in Figures 9(a) through 9(e).

Deposition in trenches with an initial catalyst coverage of 0.00054 is predicted to be conformal, as shown in Figure 9(a). Because of geometric leveling associated with the sloping sidewalls, the trench is still predicted to be filled in the absence of sidewall roughness and ignoring the cupric ion depletion associated with the increasing aspect ratio of the unfilled region. These latter effects would be expected to result in the formation of an occluded void such as that observed in the corresponding experiment (0.5-μmol/L–30-s derivatization in Figure 8).

Increasing the initial catalyst coverage an order of magnitude is predicted to result in superfilling behavior,

[1] T. P. Moffat, P. J. Chen, A. Castillo, L. Gan, C. Yang, B. Baker, D. Josell, W. F. Egelhoff, and L. Richter, unpublished results.

as shown in Figure 9(b); enrichment of the catalyst begins on the bottom corners, leading to significant acceleration of the copper deposition rate and the formation of a V-notch shape. Further enrichment accompanies the shape transition from a V-notch to a flat bottom when the opposing corners meet at the bottom. The higher catalyst coverage leads to a marked increase in the upward velocity of the bottom surface. Further increase in catalyst collection on that surface continues through accumulation of the catalyst previously adsorbed on the sidewall area being eliminated by the rapid upward motion of the bottom surface. The narrowed bottom surface is predicted to escape the trench just before impingement of the sidewalls. In practice, the very large aspect ratio of the unfilled region during the final stages of filling leads to significant cupric ion depletion that might prevent filling. This would be consistent with the cusped surface profile evident in the experimental results for the 5-μmol/L SPS–30-s derivatized electrode shown in Figure 8.

Increasing the initial catalyst coverage to 0.053 is predicted to result in near-optimal superfilling behavior, as shown in Figure 9(c). Enrichment at the bottom corners leads to rapid formation of first the V-notch and then the nearly flat bottom. As in the other simulations, the advancing bottom surface accelerates further as it collects catalyst from the eliminated sidewall areas. The accelerating bottom surface also exhibits subtle oscillations in shape associated with the continual translation of catalyst from the sidewalls to the bottom surface. The catalyst coverage approaches unity as the bottom surface reaches the top of the trench. Further deposition results in bump formation above the trench that in practice is often referred to as "momentum" plating. From this point on, the expanding surface area associated with the advancing convex section results in progressive dilution of the local catalyst coverage. The simulation also reveals the importance of catalyst dilution on the convex corners at the top of the trench during an earlier stage of feature filling; the decreasing deposition rate on these sections permits greater access of Cu^{2+} to the highly catalyzed bottom surface. This is a substantial concern, for example, for the 50-μmol/L SPS–30-s sample in Figure 8, where deposition in the field over the trench is already proceeding at $>50\%$ of the diffusion-limited current density. Significantly, this indicates that the geometrically differentiated surface reactivity predicted by the CEAC model can dominate feature filling even in the presence of a substantial metal ion concentration gradient that accompanies rapid metal deposition.

The colorized simulations of near-optimal superfilling are particularly helpful in explaining the results of postdeposition surface-analytical work on bumped surfaces. Specifically, while the catalyzed bottom surface can reach coverage values approaching unity during filling, the bottom surface at this point has yet to reach planarity with the free surface, rendering the geometry beyond the scope of conventional quantitative surface analysis. Similarly, when the feature is completely filled and better suited for postdeposition analysis, dilution effects associated with the increase in area (note the convex surface geometry) result in a lateral variation in catalyst coverage of only 0.2. Measuring such variations in surface coverage at the submicrometer level is nontrivial using most standard surface-analytical tools, possibly explaining the lack of reports detailing differences between the sulfur coverage on overfill bumps versus the neighboring planar field.

Increasing the initial catalyst coverage to 0.42 or 0.88 is predicted to result in a reversion to failure to superfill the trench [Figures 9(d) and 9(e)]. For a starting coverage of 0.42, catalyst enrichment on the advancing concave corners approaches unity, and a V-notch geometry is rapidly established in agreement with the experiment on the 500-μmol/L–30-s derivatized SPS electrodes (Figure 8). The simulation gives a clear visualization of the reason why the CEAC mechanism nonetheless fails to fill this feature. Specifically, even with near-saturation coverage attained on the advancing concave corners, the coverage on the bottom surface cannot exceed 2.5 times the starting coverage on the sidewalls. With further increases in the differential deposition rate being impossible, the sidewalls impinge before the bottom surface is able to escape the trench.

For an initial catalyst coverage of 0.88, the deposition rate is predicted to be effectively saturated near the start of metal deposition, with geometrically driven changes in catalyst coverage on the concave surfaces being minimal [Figure 9(e)]. Deposition within the trench proceeds conformally, although motion of the top convex corners of the trench is inhibited because of catalyst dilution effects described earlier.

Though not modeled here, significant depletion of the Cu^{++} ion within the trench is expected at the high catalyst coverages attained with the 500-μmol/L SPS–30-s and 1-mmol/L MPS–30-s derivatized specimens. Such depletion yields a gradient in the sidewall deposition rate, with faster deposition occurring at the top of the feature [12]. This results in earlier impingement at this location and void formation such as that observed in both experimental specimens (Figure 8) rather than the seams predicted in Figure 9. These impingement events can also lead to the formation of a new concave surface above the impinged sidewalls, such as that visible in Figure 9(e), at which catalyst enrichment (and dilution once the surface inverts) can again occur through the CEAC mechanism.

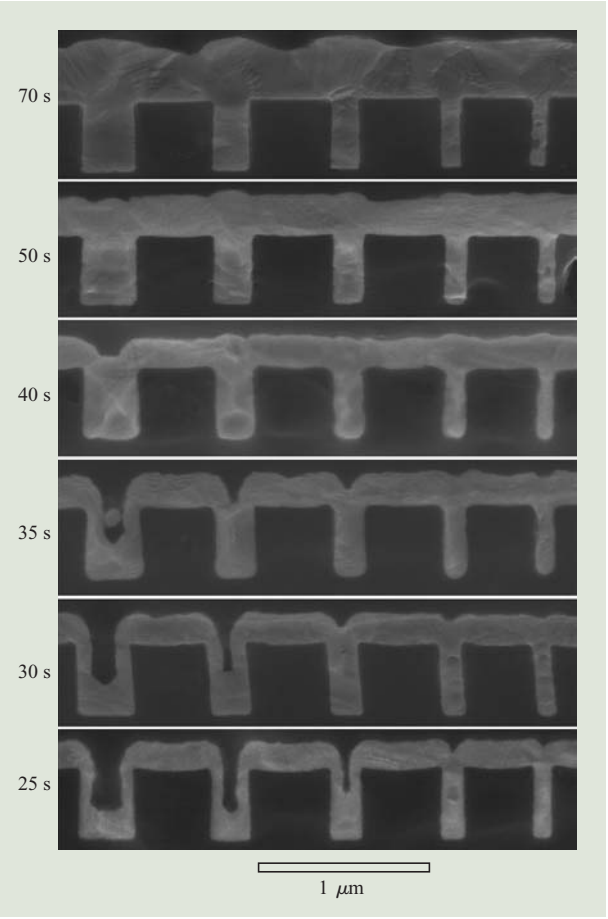

Figure 10

SEM images of shape evolution accompanying trench filling. The trench widths are 350 nm, 250 nm, 200 nm, 150 nm, and 100 nm from left to right. For these processing conditions, robust superfilling was limited to an aspect ratio of less than 2.

Superconformal deposition in an SPS–PEG–Cl electrolyte

In conventional damascene processing, electroplating is performed in an electrolyte containing both an inhibitor and a catalyst. Galvanostatic control is used in many commercial processes, and programs implementing controlled variation of current (e.g., current stepping, with lower starting currents) have also been implemented. The direct objective of such a process is repair of seed layers prior to superfilling. Nonetheless, it should be recognized that such growth programs can also result in uptake of adsorbed catalyst prior to significant metal deposition in a manner analogous to the electrode-derivatization experiments described in the previous section.

In contrast to industrial practice, potentiostatic regulation was used for this study. This avoids the ambiguity of interpreting the spatially varying current distribution within the filling features that is inherent in the superfill process, and permits unambiguous control of the reaction supersaturation and associated surface chemistry. Trench- and via-filling experiments were performed by immersion of wafer fragments in the SPS–PEG–Cl electrolyte containing 6.4-μmol/L SPS with the –0.25 V growth potential already applied. The experiments are compared with shape-change simulations.

Trench-filling experiments

Interface evolution during copper deposition in trenches of differing aspect ratio is shown in **Figure 10**. The substrates were silicon wafer fragments that had been patterned using standard electron beam lithography of spin-coated PMMA and coated with a copper seed layer using electron beam evaporation. The trenches were about 400 nm in height and 350, 250, 200, 150, and 100 nm in width, corresponding respectively to aspect ratios of 1.14, 1.67, 2.0, 2.67, and 4.0. Each specimen contained six groups of this five-trench pattern, and each specimen was repolished and examined by FE–SEM three times; in combination this provided a total of eighteen cross sections of each size feature for analysis, allowing a preliminary assessment of repeatability. In contrast to the electroanalytical experiments, these specimens were suspended in the electrolyte by hand during metal deposition. As a consequence one would not expect a steady-state boundary layer to form, owing to uncontrolled specimen motion. Nevertheless, the images of Figure 10 reveal a sequence of interface morphologies that are quite similar to those observed in the derivatization experiments and simulations shown in Figures 8 and 9, respectively.

Examination of the deposition in the 350-nm-wide trench at 25 s reveals the development of a 45° slope at the bottom corners, the earliest stage of superfilling. By 30 s the 45° corner segments have reached one another at the bottom, forming a V-notch. This is followed by the creation and subsequent rapid advance of a new bottom surface that is approaching the field by 40 s. Continued growth reveals an inversion of curvature over the feature by 50 s and significant bump formation above the trench by 70 s.

Temporal evolution of the 250-nm feature is qualitatively similar. The movement of the catalyst-enriched bottom surface between 30 s and 35 s is more rapid, transiting almost half the trench height in this period. Only minor sidewall motion is evident. The same transition appears to have occurred in the 200-nm-wide trench between 25 s and 30 s. Shorter deposition times are required to assay the filling of the small features.

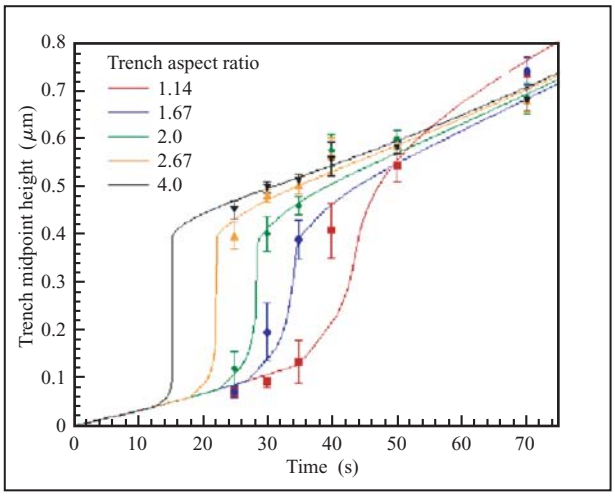

Figure 11

Trench-filling experiments compared with shape-change simulations by tracking the evolving interface position along the trench centerline. A vertical transition, such as is evident at ≈15 s for trenches with an aspect ratio of 4, indicates seam or void formation.

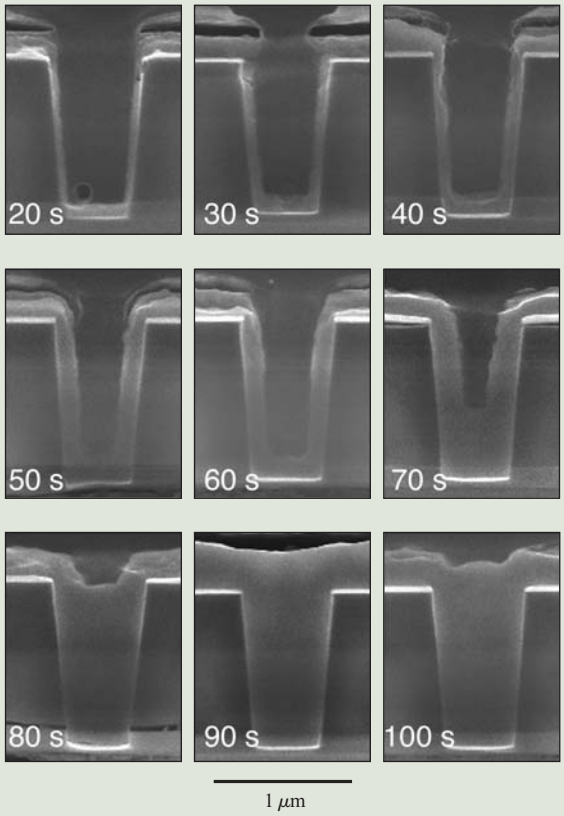

Figure 12

Time sequence showing bottom-up superfilling of vias using the same processing conditions as in the trench-filling experiments shown in Figure 10.

Nonetheless, examination of the full array of specimens reveals several voids in the finer features, one of which is visible at the top of the 200-nm-wide trench. This suggests that superfilling occurs only in trenches with an aspect ratio ≤ 2 for these conditions.

The time-dependent filling of the full range of feature sizes is summarized in **Figure 11** by plotting the height of the trench bottom on the midline of the feature as a function of the deposition time. The error bars represent the standard deviation of the measurements on the eighteen specimens.

Simulation of trench filling

The morphological evolution accompanying trench superfilling during concurrent catalyst accumulation and copper deposition (Figure 10) is qualitatively indistinguishable from that observed during the filling of specimens that were derivatized with catalyst prior to copper deposition (Figure 9). Shape-change simulations were obtained by implementing the CEAC mechanism using the kinetics parameters required by Equations (4) and (7), as well as the supporting equations, from Table 2 (with the exception that bulk concentrations were presumed to exist at the interface because of the uncontrolled specimen motion during the experiments). The predicted time-dependent heights of the trench bottoms on the midlines of the features are overlaid on the experimental data points in Figure 11. A vertical trajectory is synonymous with seam or void formation. Good agreement with the experiments is evident, although the simulations indicate that the threshold aspect ratio for superfilling is close to 1.6, while experiments suggest reliable filling up to an aspect ratio of 2.

Via-filling experiments

Deposition in vias, unlike trenches, is a three-dimensional problem by virtue of the nonzero curvature of the cylindrical sidewalls [47]. Filling experiments were therefore conducted on cylindrical vias 1.15 μm deep with diameters of 0.44 μm and 0.62 μm at the bottom and top, respectively. This geometry corresponds to a 4.5° slope of the sidewalls from the vertical. The wafer fragments were immersed with the −0.25-V overpotential applied and were immediately clipped to the side of the electrochemical cell in order to allow the hydrodynamic boundary layer to develop. Further experimental information is available elsewhere [47]. FE–SEM images of the via filling are shown in ten-second increments in **Figure 12**. Deposition

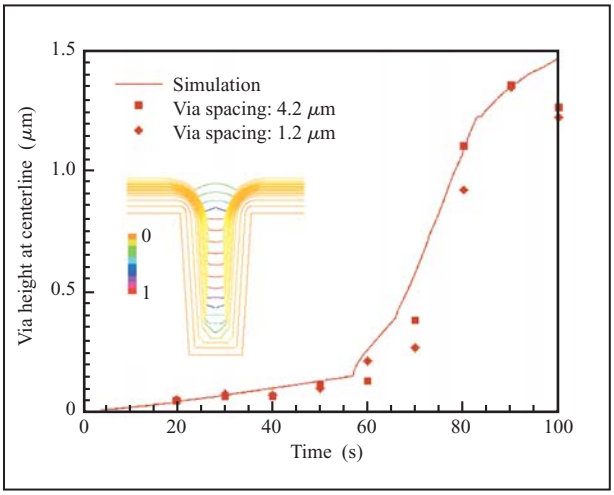

Figure 13

Tracking the interface mid-height position during via filling provides a comparison between simulation and experiment. The inset shows a colorized θ_{SPS} contour plot of simulated bottom-up film growth.

is essentially conformal for the first 60 seconds, with acceleration of the bottom surface by approximately 70 s and complete superconformal filling of the via by approximately 90 s. The filling process is summarized in Figure 12 by plotting the height of the deposit along the centerline of the via as a function of deposition time.

Simulation of via filling

The interface tracking code was used to simulate filling of the via. As with the trench simulations, depletion across the boundary layer is accounted for through Equation (14), and depletion within the feature is ignored. The solid curve in **Figure 13** corresponds to the predicted height of the via bottom on the centerline of the via. Agreement is excellent, especially considering the neglect of mass-transport-derived depletion of cupric ions within the via.

The filling contours inset in Figure 13 agree with the evidently robust bottom-up filling in the experiment shown in Figure 12. Interestingly, simulation for a vertical sidewall geometry indicates marginal superfilling, with the bottom surface only barely escaping from imminent sidewall impingement (not shown). This can be seen qualitatively through comparison of the sidewall thickness at the top of the feature prior to completion of feature filling with the width at the bottom of the feature. Thus, sidewall tilt substantially affects the observed behavior.

Summary

A quantitative connection between standard electroanalytical measurements on planar electrodes and superfilling of submicrometer features with copper has been developed. Voltammetry and chronoamperometry were used to quantify the effects of additive adsorption and consumption on copper deposition kinetics. The rate constants for both processes were found to be potential-dependent. The determined kinetic parameters were the only inputs for a CEAC-based code used to simulate feature-filling experiments. There were no adjustable parameters in the feature-filling simulations. The simulations were found to be in good agreement with three different types of feature-filling experiments.

Electrode derivatization was seen to be a powerful tool for understanding the influence of individual electrolyte additives. In particular, superfilling was demonstrated using patterned specimens that had been pretreated with a submonolayer quantity of catalyst, then plated with copper in a catalyst-free electrolyte. The agreement of shape evolution in feature-filling simulations with experimental results was just as good for those specimens as for samples filled in a single electrolyte containing both catalyst and suppressor. This work indicates the central role of catalyst surface chemistry in establishing the differential reactivity required for submicrometer-feature superfilling, demonstrating that solution-phase transport and/or homogeneous chemistry play at most only a secondary role in the experiments examined.

References

1. P. C. Andricacos, *Interface* (Electrochem. Soc.) **8**, 32 (1999).
2. P. C. Andricacos, C. Uzoh, J. O. Dukovic, J. Horkans, and H. Deligianni, *IBM J. Res. & Dev.* **42**, 567 (1998).
3. H. Deligianni, J. O. Dukovic, P. C. Andricacos, and E. G. Walton, in *Electrochemical Processing in ULSI Fabrication and Semiconductor/Metal Deposition II*, P. C. Andricacos, J. L. Stickney, and G. M. Olezak, Eds., **PV 99-9**, The Electrochemical Society Proceedings Series, Pennington, NJ, 2000, p. 52.
4. A. C. West, *J. Electrochem. Soc.* **147**, 227 (2000).
5. J. Reid and S. Mayer, in *Proceedings of the 1999 Advanced Metallization Conference*, M. E. Gross, T. Gessner, N. Kobayashi, and Y. Yasuda, Eds., Materials Research Society, Warrendale, PA, 2000, p. 53.
6. T. Ritzdorf, D. Fulton, and L. Chen, in *Proceedings of the 1999 Advanced Metallization Conference*, M. E. Gross, T. Gessner, N. Kobayashi, and Y. Yasuda, Eds., Materials Research Society, Warrendale, PA, 2000, p. 101.
7. E. Richard, I. Vervoort, S. H. Brongersma, H. Bender, G. Beyer, R. Palmans, S. Lagrange, and K. Maex, in *Proceedings of the 1999 Advanced Metallization Conference*, M. E. Gross, T. Gessner, N. Kobayashi, and Y. Yasuda, Eds., Materials Research Society, Warrendale, PA, 2000, p. 149.
8. T. P. Moffat, J. E. Bonevich, W. H. Huber, A. Stanishevsky, D. R. Kelly, G. R. Stafford, and D. Josell, *J. Electrochem. Soc.* **147**, 4524 (2000).
9. P. Taephaisitphongse, Y. Cao, and A. C. West, *J. Electrochem. Soc.* **148**, C492 (2001).
10. T. P. Moffat, D. Wheeler, W. H. Huber, and D. Josell, *Electrochem. Solid-State Lett.* **4**, C26 (2001).
11. D. Josell, D. Wheeler, W. H. Huber, J. E. Bonevich, and T. P. Moffat, *J. Electrochem. Soc.* **148**, C767 (2001).

12. D. Wheeler, D. Josell, and T. P. Moffat, *J. Electrochem. Soc.* **150**, C203 (2003).
13. A. C. West, S. Mayer, and J. Reid, *Electrochem. Solid-State Lett.* **4**, C50 (2001).
14. G. McFadden, S. R. Coriell, T. P. Moffat, D. Josell, D. Wheeler, W. Schwarzacher, and J. Mallett, *J. Electrochem. Soc.* **150**, C591 (2003).
15. B. C. Baker, C. Witt, D. Wheeler, D. Josell, and T. P. Moffat, *Electrochem. Solid-State Lett.* **6**, C67 (2003) and references therein.
16. D. Josell, S. Kim, D. Wheeler, T. P. Moffat, and S. G. Pyo, *J. Electrochem. Soc.* **150**, C368 (2003) and references therein.
17. U. Bertocci, *Electrochim. Acta* **11**, 1261 (1966).
18. A. Molodov, G. N. Markosyan, and V. V. Losev, *Electrochim. Acta* **17**, 701 (1972).
19. U. Bertocci and D. Turner, *Encyclopedia of Electrochemistry of the Elements*, Vol. 2, A. J. Bard, Ed., Marcel Dekker, New York, 1974, p. 1.
20. M. Yokoi, S. Konishi, and T. Hayashi, *Denki Kagaku* **51**, 310 (1983).
21. S. Krzewska, *Electrochim. Acta* **42**, 3531 (1997).
22. S. Yoon, M. Schwartz, and K. Nobe, *Plating & Surface Finishing* **81**, 65 (December 1994) and references therein.
23. E. Gileadi and V. Tsionsky, *J. Electrochem. Soc.* **147**, 567 (2000).
24. A. Jardy, A. Legal Lasalle-Molin, M. Keddam, and H. Takenouti, *Electrochim. Acta* **37**, 2195 (1992).
25. J. J. Kelly and A. C. West, *J. Electrochem. Soc.* **145**, 3477 (1998).
26. M. R. H. Hill and G. T. Rogers, *J. Electroanal. Chem.* **86**, 179 (1978).
27. M. Yokoi, S. Konishi, and T. Hayashi, *Denki Kagaku* **52**, 218 (1984).
28. D. Stoychev and C. Tsvetanov, *J. Appl. Electrochem.* **26**, 741 (1996).
29. J. J. Kelly and A. C. West, *J. Electrochem. Soc.* **145**, 3472 (1998).
30. T. P. Moffat, D. Wheeler, and D. Josell, *J. Electrochem. Soc.* **151**, C262 (2004).
31. M. Kang and A. A. Gewirth, *J. Electrochem. Soc.* **150**, C426 (2003).
32. S. G. Malhotra, P. S. Locke, A. H. Simon, J. Fluegel, P. DeHaven, D. G. Hemmes, R. Jackson, and E. Patton, in *Proceedings of the 1999 Advanced Metallization Conference*, M. E. Gross, T. Gessner, N. Kobayashi, and Y. Yasuda, Eds., Materials Research Society, Warrendale, PA, 2000, p. 77.
33. B. Baker, D. Pena, M. Herrick, R. Chowdhury, E. Acosta, C. R. Simpson, and G. Hamilton, in *Electrochemical Processing in ULSI Fabrication and Semiconductor/Metal Deposition II*, P. C. Andricacos, P. C. Searson, C. Reidsema-Simpson, P. Allongue, J. L. Stickney, and G. M. Oleszek, Eds., The Electrochemical Society Proceedings Series, Pennington, NJ, 1999.
34. P. C. Andricacos, C. Parks, C. Cabral, R. Wachnik, R. Tsai, S. Malhotra, P. Locke, J. Fluegel, J. Horkans, K. Kwietniak, C. Uzoh, K. P. Rodbell, L. Gignac, E. Walton, D. Chung, and R. Geffken, in *Electrochemical Processing in ULSI Fabrication and Semiconductor/Metal Deposition II*, P. C. Andricacos, P. C. Searson, C. Reidsema-Simpson, P. Allongue, J. L. Stickney, and M. Oleszek, Eds., The Electrochemical Society Proceedings Series, Pennington, NJ, 1999.
35. O. M. Magnussen, *Chem. Rev.* **102**, 679 (2002).
36. H. A. Biebuyck, C. D. Bain, and G. M. Whitesides, *Langmuir* **10**, 1825 (1994).
37. Ch. Jung , O. Dannenberger, Y. Xu, M. Buck, and M. Grunze, *Langmuir* **14**, 1103 (1998).
38. S. Vollmer, P. Fouquet, G. Witte, Ch. Boas, M. Kunat, U. Burghaus, and Ch. Woll, *Surf. Sci.* **462**, 135 (2000).
39. H. Kondoh, N. Saito, F. Matsui, T. Yokoyama, T. Ohta, and H. Kuroda, *J. Phys. Chem. B* **105**, 12870 (2001).
40. S. Driver and D. P. Woodruff, *Surf. Sci.* **488**, 207 (2001).
41. M. J. Esplandiu, H. Hagenstrom, and D. M. Kolb, *Langmuir* **17**, 828 (2001).
42. D. K. Schwartz, *Ann. Rev. Phys. Chem.* **52**, 107 (2001).
43. S. Xu, S. J. N. Cruchon-Dupeyrat, J. C. Garno, G.-Y. Liu, G. K. Jennings, T.-H. Yong, and P. E. Laibinis, *J. Chem. Phys.* **108**, 5002 (1998).
44. L. S. Jung and C. T. Campbell, *J. Phys. Chem. B* **104**, 11168 (2000).
45. M. Schweizer, H. Hagenstrom, and D. M. Kolb, *Surf. Sci.* **490**, L627 (2001).
46. T. P. Moffat, D. Wheeler, C. Witt, and D. Josell, *Electrochem. Solid-State Lett.* **5**, C49 (2002).
47. D. Josell, B. Baker, C. Witt, D. Wheeler, and T. P. Moffat, *J. Electrochem. Soc.* **149**, C637 (2002).

Received August 21, 2003; accepted for publication March 8, 2004; Internet publication December 7, 2004

Thomas P. Moffat *National Institute of Science and Technology (NIST), Materials Science and Engineering Laboratory, Building 224, Room B166, Gaithersburg, Maryland 20899 (thomas.moffat@nist.gov).* Dr. Moffat is a member of the Electrochemical Processing Group in the Metallurgy Division at the National Institute of Standards and Technology (NIST). He received B.E. and M.Sc. degrees in materials science and engineering from Vanderbilt University in 1982 and 1984, respectively, and an Sc.D. degree in materials science and engineering from the Massachusetts Institute of Technology in 1989. He then spent two years as a postdoctoral associate in A. J. Bard's laboratory at the University of Texas, Austin. Dr. Moffat joined NIST in 1991 to study thin-film deposition processes. In 2001 he received the Gold Medal of the U.S. Department of Commerce for his work in the area of superconformal film growth. He is an author or coauthor of more than 75 technical papers. Dr. Moffat is an active member of the Electrochemical Society, the International Society of Electrochemistry, the Materials Research Society, and the American Association for the Advancement of Science.

Daniel Wheeler *National Institute of Science and Technology (NIST), Materials Science and Engineering Laboratory, Building 223, Room A3l3, Gaithersburg, Maryland 20899 (daniel.wheeler@nist.gov).* Dr. Wheeler is a guest researcher in the Materials Structure and Characterization Group in the Metallurgy Division at NIST. He conducted his studies in the United Kingdom, receiving B.Sc. and M.Sc. degrees in mathematics from Imperial College in 1994 and 1995, respectively, and a Ph.D. degree in computational mechanics from Greenwich University in 2000. After completion of his Ph.D. degree, he joined NIST to work in the Center for Computational and Theoretical Material Science with the Solder Interconnect Design Group. Dr. Wheeler specializes in numerical analysis for interpreting experimental results. He has published papers explaining the relationship between the geometry and self-alignment forces of flip-chip solder joints in addition to his work quantifying superconformal deposition processes. Dr. Wheeler has authored or coauthored more than 25 technical papers.

Monica D. Edelstein *National Institute of Science and Technology (NIST), Electronics and Electrical Engineering Laboratory, Building 225, Room B326, Gaithersburg, Maryland 20899 (monica.edelstein@nist.gov).* Ms. Edelstein is a member of the Semiconductor Electronics Division at NIST. She received an A.A. degree in computer science from Montgomery College in 1988 and is currently pursuing a Bachelor of Electrical Engineering degree from Johns Hopkins University. She joined NIST in 1988 to assist in the electrical and materials characterization of silicon-on-insulator (SOI) wafers, specializing in scanning electron microscopy techniques; she is currently working in the Division's Dielectric Reliability Metrology and Nanoelectronic Device Metrology programs.

Daniel Josell *National Institute of Science and Technology (NIST), Materials Science and Engineering Laboratory, Building 223, Room A158, Gaithersburg, Maryland 20899 (daniel.josell@nist.gov).* Dr. Josell is a member of the Materials Structure and Characterization Group in the Metallurgy Division at NIST. He received an A.B. degree, *summa cum laude,* in physics and mechanical engineering from Harvard College in 1987, and M.S. and Ph.D. degrees in 1989 and 1992, respectively, specializing in materials science as a Fannie and John Hertz Foundation Fellow, from Harvard University. He spent the following two years as a National Research Council postdoctoral researcher at NIST before joining the staff in 1994. For the past four years, he has studied superconformal film growth, receiving the Gold Medal of the U.S. Department of Commerce in 2001 for his work in this area. His research interests also include mechanical and thermal transport properties of multilayered materials, as well as the thermodynamics of interfaces and their impact on the stability of multilayered structures. Dr. Josell is the author or a coauthor of more than 75 technical papers; he is a member of the Materials Research Society.